Automated Total-body PET Image Processing and Kinetic Modeling with the TURBO Toolbox

Jouni Tuisku*[1,2], Santeri Palonen*[1,2], Henri Kärpijoki[1,2], Aino Latva-Rasku[1,2], Nelli Tuomola[1,2], Harri Harju[1,2], Sergey Nesterov[1,2], Vesa Oikonen[1,2], Hidehiro Iida[1,2], Jarmo Teuho[1,2], Chunlei Han[1,2], Tomi Karjalainen[1,2], Anna K. Kirjavainen[1,4], Johan Rajader[1,3], Riku Klen[1,2], Pirjo Nuutila[1,2], Juhani Knuuti[1,2], Lauri Nummenmaa[1,2,5]

[1]Turku PET Centre, University of Turku, Turku, Finland
[2]Turku PET Centre, Turku university hospital, Turku, Finland
[3]Turku PET Centre, Accelerator Laboratory, Åbo Akademi University, Turku, Finland
[4]Turku PET Centre, Radiopharmaceutical Chemistry Laboratory, University of Turku, Turku, Finland.
[5]Department of Psychology, University of Turku, Turku, Finland

*contributed equally to this study

Keywords: [^{15}O]H_2O, [^{18}F]FDG, automated processing, kinetic modelling, pipeline

ABSTRACT
Total-body PET imaging is a novel concept that requires a high level of automatization and standardization, as the large number of target tissues increases manual workload significantly. We introduce an automated analysis pipeline (TURBO) for preprocessing and kinetic modeling of total-body [^{15}O]H_2O and [^{18}F]FDG PET data, enabling efficient and reproducible analysis of tissue perfusion and metabolism at regional and voxel level. The approach employs automated CT segmentation for ROI delineation, image-derived input determination, and region-specific PET data kinetic modelling.

Methods: We validated the analysis pipeline using Biograph Vision Quadra (Siemens Healthineers) total-body PET/CT scans from 21 subjects scanned with [^{15}O]H_2O and 16 subjects scanned with [^{18}F]FDG using six ROIs (cortical brain gray matter, left iliopsoas, right kidney, pancreas, spleen and liver) representing different levels of blood flow and glucose metabolism**.**

Results: Model fits showed good quality with consistent parameter estimates at both regional and voxel levels ($R^2 > 0.91$ for [^{15}O]H_2O, $R^2 > 0.99$ for [^{18}F]FDG). Estimates from manual and automated input functions were correlated ($R^2 > 0.86$ for [^{15}O]H_2O, and $R^2 > 0.88$ for [^{18}F]FDG) with minimal bias (<10% for [^{15}O]H_2O and <2% for [^{18}F]FDG). Manually and automatically (CT-based) extracted ROI level data showed strong agreement ($R^2 > 0.82$ for [^{15}O]H_2O and $R^2 > 0.83$ for [^{18}F]FDG), while motion correction had little impact on parameter estimates ($R^2 > 0.83$ for [^{15}O]H_2O and $R^2 > 0.88$ for [^{18}F]FDG) compared with uncorrected data.

Conclusion: Our automated analysis pipeline provides reliable and reproducible parameter estimates across different regions, with average processing time of <180 min per subject. This pipeline completely automatizes total-body PET analysis, reducing manual effort and enabling reproducible studies of inter-organ blood flow and metabolism, including brain-body interactions.

INTRODUCTION

Long axial field of view (LAFOV) PET scanners present unique opportunities for scientific research and clinical diagnostics by enabling the simultaneous, noninvasive imaging of multiple organs and their physiological interactions. These systems provide clear benefits, including improved count sensitivity, extended image coverage, and extraction of image-derived input function from aorta (Knuuti et al., 2023). However, they also introduce new challenges for data analysis. Patient movement is a major concern in LAFOV studies, as complete patient restraining is not possible similarly as e.g. in brain-only studies. In addition, manual pre-processing of total-body PET data is time-consuming, especially when analyzing multiple tissues. One LAFOV study may contain tens of different regions of interest (ROI), whose delineation alone can exceed a full workday per subject. Furthermore, manual approach is prone to operator bias, which may reduce reproducibility compared to automated methods (Karjalainen et al., 2020). Finally, the complex preprocessing, modelling and data analysis flow warrants comprehensive quality control to ensure accurate outputs at all stages and again, completing all these steps by human operators is simply not feasible.

Any all-inclusive total-body PET processing pipeline should handle preprocessing, region of interest (ROI) delineation, and kinetic modeling using various approaches tailored to different radiotracers – making the development of a comprehensive PET pipeline a challenging task. While various tools exist for automated brain PET data analysis (Funck et al., 2018; Greve et al., 2014; Gunn et al., 2016; Karjalainen et al., 2020), equivalent pipelines for total-body PET data are not yet widely available. To address these issues, we introduce a novel open-source Turku Total-Body PET modelling pipeline (TURBO), which enables automated and reproducible processing and kinetic modeling of total-body data. It supports various radiotracers and kinetic models and allows fully automated processing, including coregistration, motion correction, input function determination, and ROI delineation. The pipeline enables both regional and voxel-level kinetic modeling, with the flexibility to apply tissue-specific models, and provides visual and numerical tools for quality control of preprocessing steps.

Here, we describe and validate the TURBO pipeline (freely available at https://turbo.utu.fi) using [^{15}O]H_2O and [^{18}F]FDG PET data to benchmark preprocessing and modeling of tissue perfusion and glucose metabolism. We compared automated image derived input function (IDIF) with the manually delineated input, assessed results with and without motion correction, evaluated the results of ROI-based and voxel-level kinetic modelling, and compared outcome measures from manually and automatically determined ROIs. We hypothesized that TURBO provides rapid, accurate and reproducible approach for modelling total-body PET perfusion and metabolism data at voxel and regional levels.

MATERIALS AND METHODS

Overview of TURBO pipeline

TURBO (TURku total-BOdy) pipeline runs on MATLAB (The MathWorks, Inc., Natick, MA, USA), and utilizes openly available tools for data processing. For all PET kinetic modelling, we use matlab implementations of openly available and previously validated in-house software (http://www.turkupetcentre.net/petanalysis). The general framework involves CT to PET registration, PET motion correction, segmentation of the CT image into tissues and organs, automatic image-based input extraction and finally, kinetic modelling in regional

and voxel level. The pipeline outputs total-body parametric images, separate parametric brain images normalized to MNI space, regional outcome measures as well as quality control metrics. Overview of the workflow is shown in **Figure 1**, and detailed process documentation is described at https://turbo.utu.fi.

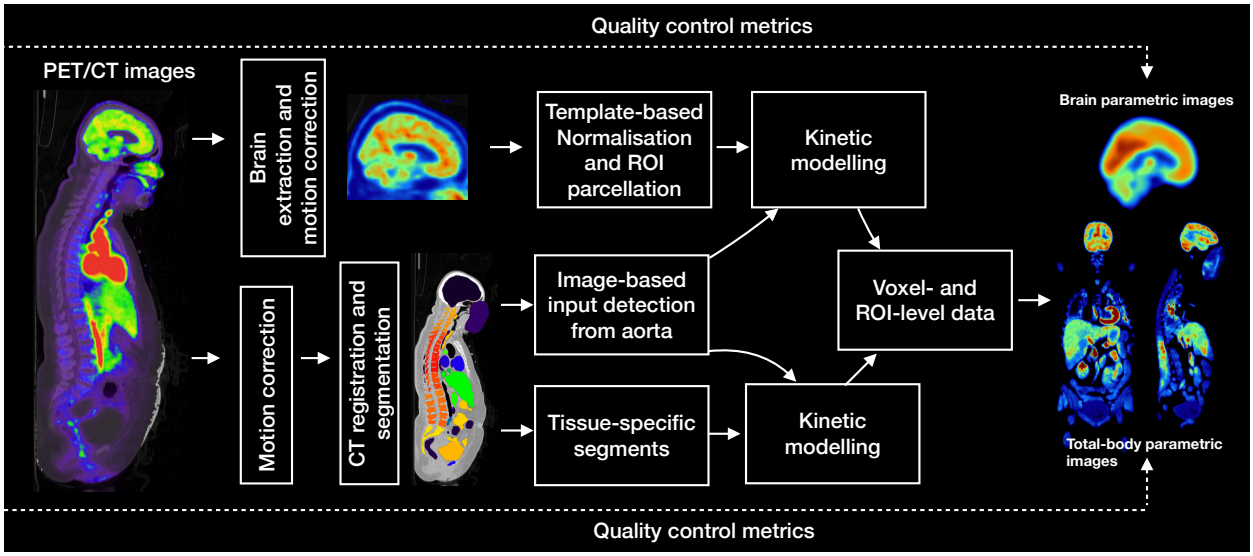

Figure 1. Flowchart for the TURBO pipeline.

Total-body PET data preprocessing

The process begins by converting DICOM images to NIfTI using the *dcm2niix* tool (Li et al., 2016), and extracting required metadata such as framing, injected dose, and subject weight from the DICOM header. Next, PET data are corrected for subject motion following previously described approach (Sundar et al., 2023), that employs diffeomorphic *greedy* registration algorithm (https://greedy.readthedocs.io). For [^{18}F]FDG, the motion correction start frame is determined by normalized cross-correlation (NCC), as described in (Sundar et al., 2023). In our [^{18}F]FDG validation data this varies between 4 - 6 min. Due to the variation in [^{15}O]H_2O distribution, early frames are discarded, and the start frame is selected as the time point where the heart time-activity curve (TAC) falls below half of its peak value (this varies between 15 – 45 s in our validation data). For both radioligands, the motion correction reference frame is selected as the one with the highest NCC relative to the CT. In our [^{15}O]H_2O validation data, this frame is typically near the scan midpoint and in [^{18}F]FDG data near the scan endpoint. Subsequently, CT is registered with the PET mean image using the greedy algorithm to correct any misalignments and ensuring that CT-based regions of interest (ROIs) correspond with the PET data. The CT image is resampled to PET voxel size, whereafter the *TotalSegmentator* tool (Wasserthal et al., 2023) is used for CT-based segmentation of major organs and tissues, to serve as ROIs for PET quantification.

Image derived input extraction

Because the total-body PET image covers the heart in addition to other targets of interest, input function can be determined from the images. For automatic IDIF determination, a separate cropped PET image containing heart and aorta is extracted from the original total-body PET image and corrected for motion using rigid motion correction method (Nordstrom et al., 2024), which enables motion correction also for the initial frames. Consequently, IDIF is extracted from descending aorta following the standard criteria for manual input

delineation in our centre: The lower third of myocardium is used as a higher landmark, from which the maximums are located and connected transaxially by gap filling algorithm 10 cm downwards. (**Figure 2 A-B**).

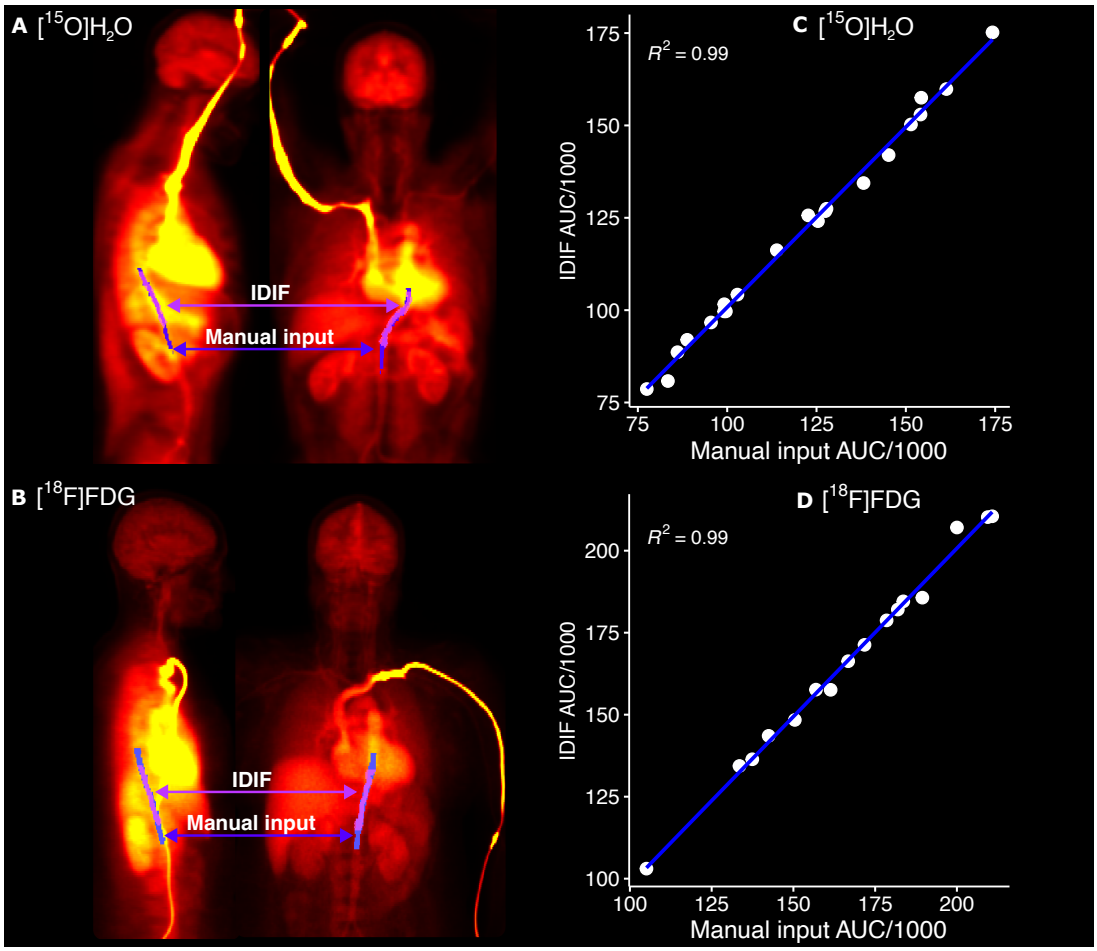

Figure 2. A-B) Manually delineated descending aorta ROI (blue) overlaid with image derived input (violet) for [^{15}O]H_2O and for [^{18}F]FDG. **C-D)** Scatterplots of areas under the input curves of manually delineated descending aorta and image derived input for [^{15}O]H_2O and for [^{18}F]FDG.

Brain-PET data analysis

The brain consists of distinct cytoarchitectonical and functionally separable regions, which are previously defined in various atlases in standard stereotactic space. Therefore, a separate analysis pathway is used to incorporate these atlases and to facilitate whole-brain analysis using widely used toolboxes (e.g., SPM, FSL) based on parametric mapping of spatially normalized brain images. In this stream, in-house Magia-toolbox (Karjalainen et al., 2020) is used for extracting brain from the original PET image, followed by rigid motion correction and spatial radioligand template-based normalization for transforming the desired atlas from standard MNI space to the subject native space. The pipeline includes the ROIs from AAL-atlas (Tzourio-Mazoyer et al., 2002) containing cortical lobes and selected subcortical regions, but any other atlas in MNI space can also be used. Finally, kinetic modelling (see below) is carried out for each region, as well as in voxel level for the whole brain data.

Total-body [^{15}O]H_2O PET data modelling

For [^{15}O]H_2O, one-tissue compartmental model (1TCM) (Kety and Schmidt, 1948) is fitted for each measured regional time activity curve. The model is defined using the following equations (see supplementary material for details):

$$C_{\mathrm{T}}(T) = K_1 \int_0^T C_{\mathrm{A}}(t) - k_2 \int_0^T C_{\mathrm{T}}(t) \quad (1)$$

$$C_{\mathrm{PET}}(t) = C_{\mathrm{T}}(t) + V_{\mathrm{A}} C_{\mathrm{A}}(t) \quad (2)$$

where C_{PET} is the measured PET activity concentration, C_T is the tissue activity concentration, C_A is the arterial activity concentration corrected for radiotracer delay in tissue, V_A is the arterial volume fraction, K_1=f describes the blood flow, and k_2=f/p, where p=K_1/k_2 is the partition coefficient of water (i.e. distribution volume).

Because the standard 1TCM model fitting with descending aorta IDIF is not feasible in liver, the arterial and portal vein blood flow fractions $r_a = f_a/(f_a + f_p)$ and $r_p = f_p/(f_a + f_p)$ (Ziegler et al., 1996) are first estimated using the dual-input model (Kudomi et al., 2008) with the descending aorta IDIF C_{IDIF} and a portal vein input curve C_{PV} (that is estimated using C_{IDIF}). Consequently, the resulting combined input

$$C_{\mathrm{liverIF}}(t) = r_{\mathrm{a}}\, C_{\mathrm{IDIF}}(t) + r_{\mathrm{p}}\, C_{\mathrm{pv}}(t)$$

is used for estimating liver parameters with the standard 1TCM.

Voxel-level [^{15}O]H_2O quantification is carried out using non-negative least squares (NNLS, Lawson and Hanson, 1995) either with estimating all three 1TCM model parameters (K_1, k_2, V_A), or basis function approach (Kudomi et al., 2009), where discrete k_2 values are used for calculating the basis functions, and K_1, V_A are estimated with NNLS (see supplementary material for model equations). For both voxel-level methods, the radiotracer delay parameter is estimated separately for each voxel, except in liver with combined input, where the input and the delay are obtained from the ROI-level quantification.

Total-body [^{18}F]FDG PET data modelling

To quantify glucose metabolism using [^{18}F]FDG, the descending aorta IDIF is first converted to plasma (Phelps et al., 1979) using the individual hematocrit measurement, after which regional and voxel-level patlak-plot (Patlak et al., 1983), fractional uptake ratio (FUR) and standardised uptake value (SUV) estimates can be calculated similarly in all regions. Because different values for lumped constant are commonly used for different organs, the glucose uptake conversion is currently omitted by default in the automated processing but can be defined by the user on tissue-by-tissue basis if needed.

After voxel-level modelling, the parametric maps are clustered into three subregions within selected areas using hierarchical clustering. This supports regional analysis of functionally distinct areas, such as kidney cortex and medulla or brain grey and white matter. Additionally, the CT-based ROIs can be trimmed by removing a specified distance from their edges to reduce signal contamination from nearby high intensity areas, or due to motion. For instance, it may be necessary to exclude spill-in from the cardiovascular system in the segmented liver.

Output
As a final step in the processing, the parameter estimates, CT-based ROI volumes, and model goodness of fit metrics (Pearson's R^2) are saved for each region in standard format. These results can then be retrieved for selected subjects using a dedicated function. Regional results from voxel-level parameter maps and from clustered regions can also be collected similarly.

Also, quality control plots illustrating the CT to PET registration, corrected PET motion, regional model fits and overlay-images of CT and voxel level parameters are saved in html-file for later visual check (see supplementary material for quality control output for representative cases of $[^{15}O]H_2O$ and $[^{18}F]$FDG).

Validation

For validation purposes in the main report, we chose six ROIs (cortical brain gray matter (GMctx), left iliopsoas, right kidney, pancreas, spleen and liver) representing different levels of blood flow, quantified as K_1 adjusted for the vascular contribution ($K_1(1-V_A)$), and glucose metabolism, quantified as patlak K_i. The results from all other segmented regions (n=72; ribs and vertebrae are excluded for clarity), are shown in the supplementary material. Because the dual input $[^{15}O]H_2O$ model in liver may have parameter identifiability issues in K_1 and k_2 parameters, we replicated the outcomes using distribution volume K_1/k_2 (see supplementary material for results).

We validated the automated $[^{15}O]H_2O$ and $[^{18}F]$FDG analysis pipeline by comparing automatically and manually derived input functions, assessing agreement between regional and voxel-level modeling, evaluating the effect of motion correction, and comparing results from manual and automatic ROI delineation. The accuracy of the automatically derived descending aorta IDIF was tested by comparing the model parameter estimates from segmented CT-based ROIs using both automated and manually drawn input, which was delineated using the above described criteria with Carimas software (Rainio et al., 2023). Agreement between regional and voxel-level estimates was evaluated by comparing parameters estimated from averaged regional TACs to voxel-wise estimates which were averaged within each ROI. To assess the motion correction, parameter estimates from motion corrected and uncorrected data were compared using CT-based ROIs. Finally, using descending aorta IDIF, the modelling results from three manually drawn axial ROIs (in liver, kidney cortices, and spleen) for $[^{15}O]H_2O$ and two ROIs (iliopsoas and liver) for $[^{18}F]$FDG were compared with the corresponding results from automatically segmented CT-based ROIs. Since the manually drawn ROIs were substantially smaller than the automatically segmented ones, we also compared the voxel-level results using manual ROI in spleen and liver with results from CT-based ROIs where the volume was reduced (20 mm from the ROI borders in liver and 10 mm in spleen). Similarly in the kidneys, the manual ROI results were compared with functionally distinct PET-based cluster in kidney cortex, and in the brain, where PET-based cortical GM cluster results were compared with results from the corresponding AAL-atlas ROI from the PET-template-based brain processing. For $[^{15}O]H_2O$, we compared also myocardial blood flow (MBF) measured as k_2 with descending aorta IDIF to manually assessed MBF using Carimas software with left ventricle input (Nesterov et al., 2009).

All regional $[^{15}O]H_2O$ parameter estimates were calculated using non-linear least squares estimation with 100 randomly initialized parameters from following lower and upper bounds: K_1:[0, 1800] ml/(min*dl), K_1/k_2:[0, 1], V_A:[0, 0.8]. Voxel-level $[^{15}O]H_2O$ parameters were

estimated using 500 basis functions with uniformly distributed k_2 values from the range [0, 6] 1/min.

Validation Data

The automated processing and kinetic total-body modelling for perfusion imaging was validated using total-body [^{15}O]H_2O PET data from 21 healthy subjects, which were acquired at Turku PET centre with Biograph Vision Quadra (Siemens Healthineers) total-body PET/CT scanner with spatial resolution of 3.3-3.8 mm FWHM and an axial field of view of 106 cm (Prenosil et al., 2022). Validation for imaging the glucose metabolism was carried out using [^{18}F]FDG PET data from healthy control and obese subjects (n=16). Data acquisition details are described in the supplementary material. The study was approved by the institutional ethical review board and conducted following the principles of the Declaration of Helsinki. All participants provided written informed consent prior to the examinations. The subject's demographic details are listed in **Table 1**.

Table 1. Study sample characteristics.

Demographic	[^{15}O]H_2O	[^{18}F]FDG
n (Males/Females)	8 / 13	4 / 12
Age y (mean ± sd)	65.4 ± 8.9	38.0 ± 7.0
Dose MBq (mean ± sd)	359.6 ± 23.8	171.8 ± 8.8
BMI kg/m2 (mean ± sd)	28.0 ± 4.9	30.6 ± 9.2

Statistical methods

All statistical comparisons were carried out in R (version 4.4.1) using Pearson's correlation and Bland-Altman analysis describing the relative difference and 95% limits of agreement between the methods.

RESULTS

Processing time:

Typical total running time for processing one subject using one CPU (CT segmented using GPU) was 160 min for [^{15}O]H_2O data, and 115 min for [^{18}F]FDG data (**Supplementary Table 1)**.

Model fits

Visual inspection indicated good model fits in in all regions, except in kidneys, where the model underestimated the measured TAC in the latter part of scan. There was a moderate variability between subjects, but data and model fits had high correlation across subjects (mean $R^2 > 0.88$ for [^{15}O]H_2O, and mean $R^2>0.92$ for [^{18}F]FDG) in all studied regions (**Figure 3**).

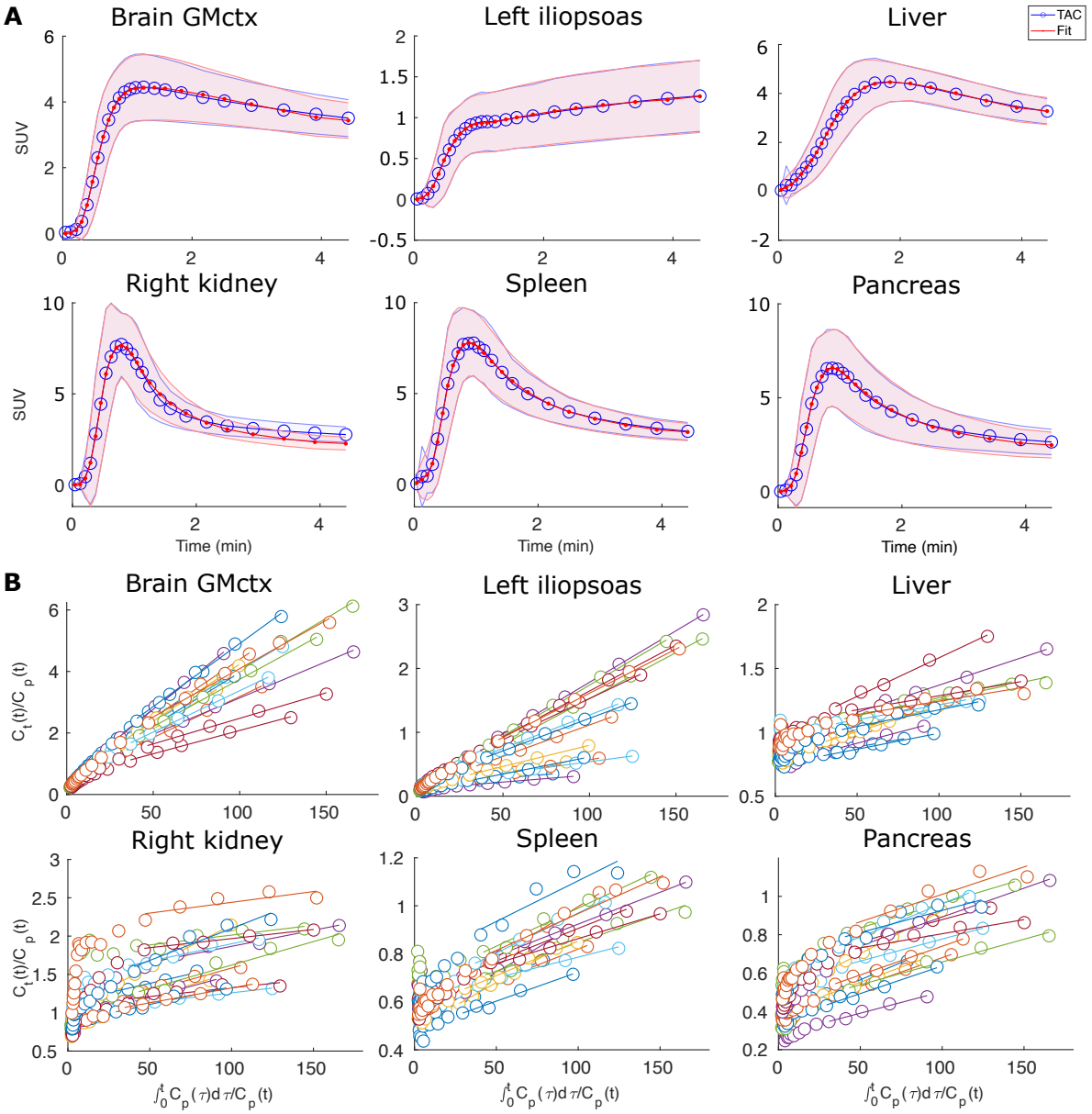

Figure 3. **A)** Between subject mean [^{15}O]H_2O PET time-activity curves (blue) and the mean one tissue compartment model fits (red) in brain cortical gray matter (GMctx), left iliopsoas, liver, right kidney, spleen and pancreas for 21 subjects scanned at rest. Shaded areas illustrate the standard deviation of the data and the corresponding model fits. **B)** [^{18}F]FDG patlak-plots in GMctx, left iliopsoas, liver, right kidney, spleen and pancreas for 16 subjects.

Automated versus manual ROI delineation

There was moderate overlap between the manually drawn and automatically derived input function mask images for both datasets, and in [^{18}F]FDG data the manual input volume was larger compared to IDIF (**Suppelmentary Table 2**). Despite this, the between the areas under the curves (AUCs) of manually derived input function and IDIF (**Figure 2 C-D**) were almost perfectly correlated (R^2=0.99).

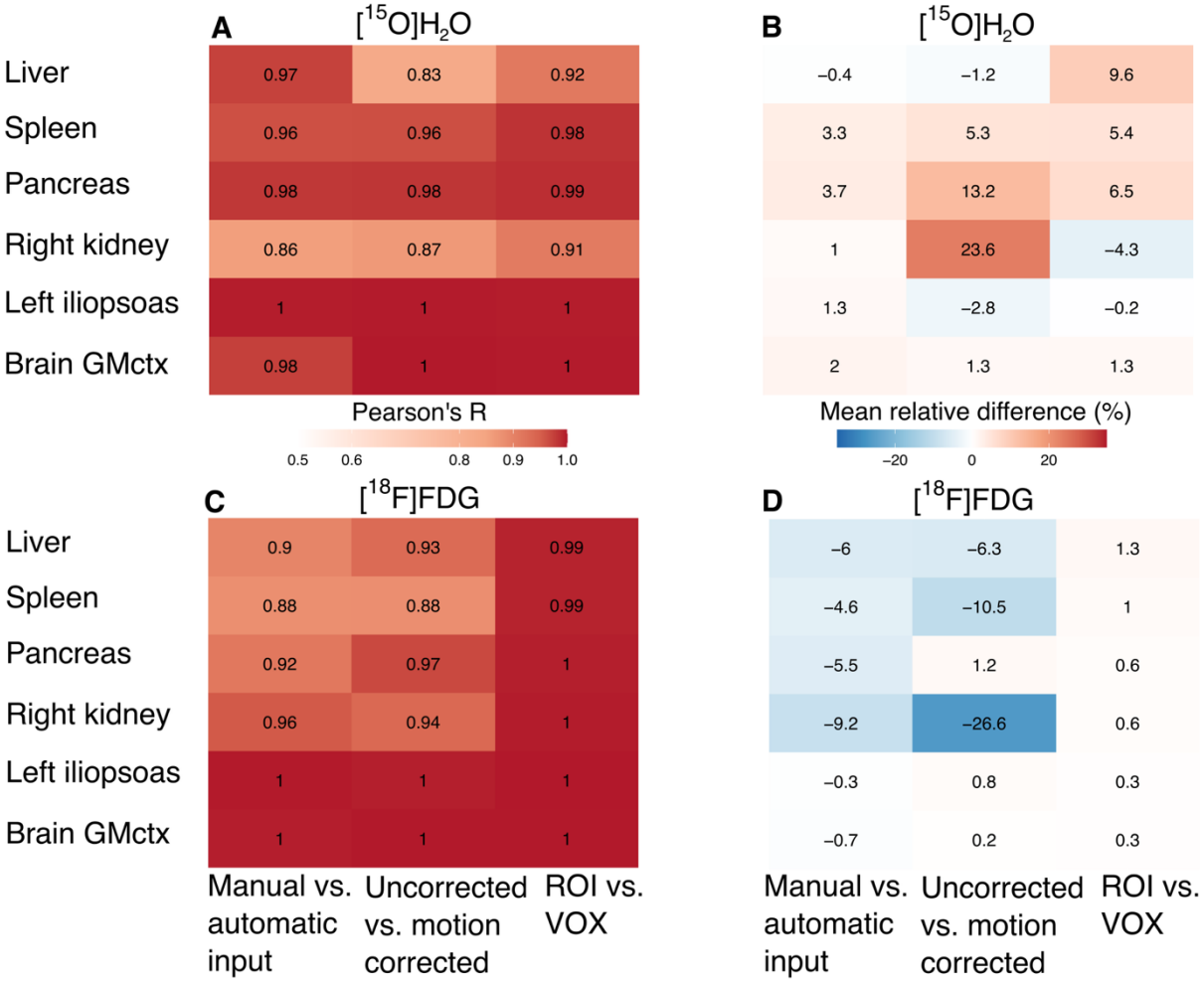

Figure 4. Comparisons between manual vs. automatic input determination methods, motion corrected and uncorrected data, and regional versus voxelwise (ROI vs. VOX) methods**. A)** Correlation coefficients (Pearson's R) and **B)** mean relative regional differences (%) of regional $[^{15}O]H_2O$ parameter estimates. **C)** Correlation coefficients (Pearson's R) and **D)** mean relative regional differences (%) of regional $[^{18}F]FDG$ K_i.

The parameter estimates using manual and automatically derived input functions had high correlation (R^2>0.97 for $[^{15}O]H_2O$, and R^2>0.91 for $[^{18}F]FDG$) in all selected six regions, with negligible bias for both radioligands (**Figure 4: manual vs. automatic input, supplementary information Figure S1**). When all regions were considered, the correlation and bias estimates were comparable in the analyzed regions, but lower correlation and higher mean relative difference was observed in arteries and in heart and lung subregions **(supplementary information Figure S2).**

Motion correction

To estimate segment-wise motion for each subject, we tracked the Euclidean distance of a single voxel, located at the mean of x-, and the maximum of y-, and z-coordinates in each segment, between the data with and without motion correction, and the results of corrected frame-wise motion for each ROI are summarized in **Supplementary Table 3**. Despite of the motion, parameter estimates using motion corrected data had high correlation (R^2>0.83 for $[^{15}O]H_2O$, and R^2>0.88 for $[^{18}F]FDG$) with the estimates obtained using uncorrected data

(**Figure 4: uncorrected vs. motion corrected**). The mean relative difference varied by region, with higher difference in right kidney (24%) and in pancreas (13%) in [^{15}O]H_2O data and in the right kidney (-27%) and in spleen (-11%) in [^{18}F]FDG data, compared to the other selected regions. When all regions were considered, lower correlation and higher mean relative difference were found mainly in arteries and in heart **(supplementary information Figure S3).**

Regional versus voxel-level results

Results for regional and voxel level modelling were almost perfectly correlated for both radioligands (**Figure4: ROI vs. VOX, Figure 5)**. The mean relative difference between regional and voxel level [^{18}F]FDG modelling was less than 2%, and below 10% for [^{15}O]H_2O When all regions were considered, lower correlation and higher mean relative difference were observed only in [^{15}O]H_2O data in arteries, lungs and in heart **(supplementary information Figure S4).**

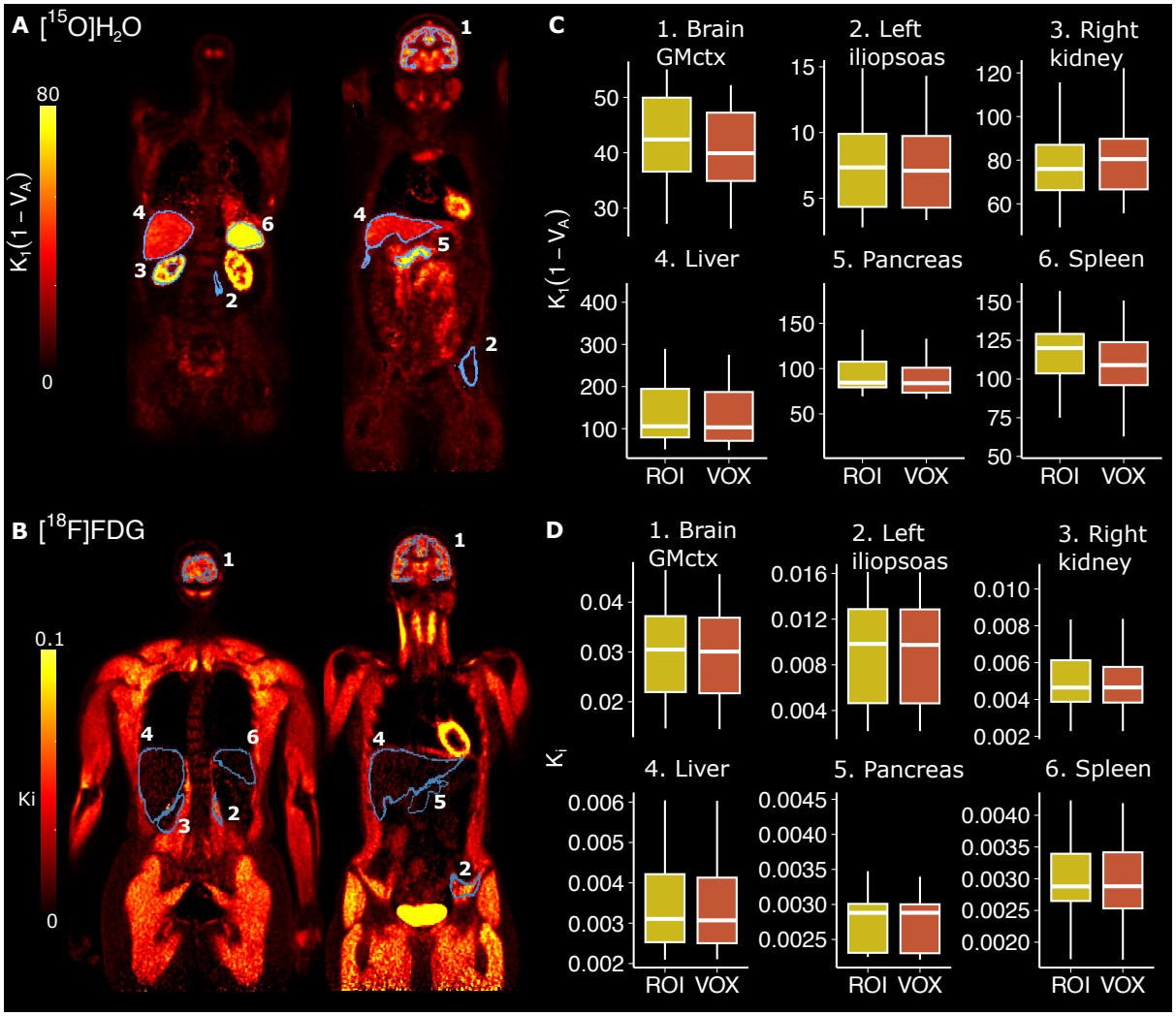

Figure 5. Voxel level average intensity projection images for representative subjects. **A)** $K_1(1\text{-}V_A)$ image for [^{15}O]H_2O and **B)** K_i image for [^{18}F]FDG. **C-D)** Boxplots illustrating the regional (ROI) and voxel level (VOX) estimates in brain cortical gray matter (GMctx), left iliopsoas, right kidney, spleen and pancreas for [^{15}O]H_2O (n=21) and [^{18}F]FDG (n=16) data.

Voxel-level results obtained using basis function method yielded higher correlation, and less bias with the ROI-level modelling results compared to the results of voxel-level model, where all three parameters were estimated **(supplementary information Figure S5)**.
Liver distribution volumes (K_1/k_2) showed similar results in all validation tests 1-3, as compared with the $K_1(1\text{-}V_A)$ estimates (**supplementary information Figure S6**), but with significantly lower coefficient of variation (6.8% in K_1/k_2 vs. 65.8% in $K_1(1\text{-}V_A)$)

Manually drawn ROIs were substantially smaller than the automatically segmented CT-based ROIs (**Supplementary Table 4)**. However, comparison between $[^{15}O]H_2O$ and $[^{18}F]$FDG parameter estimates from manually delineated ROIs and segmented CT ROIs showed high correlation (R^2>0.82 for $[^{15}O]H_2O$, and R^2>0.83 for $[^{18}F]$FDG), but moderate mean relative differences (18% in kidney, 21% in spleen, 10% in liver and 8% in myocardium for $[^{15}O]H_2O$, and -19% in liver and 7% in iliopsoas for $[^{18}F]$FDG; **Figure 5**).

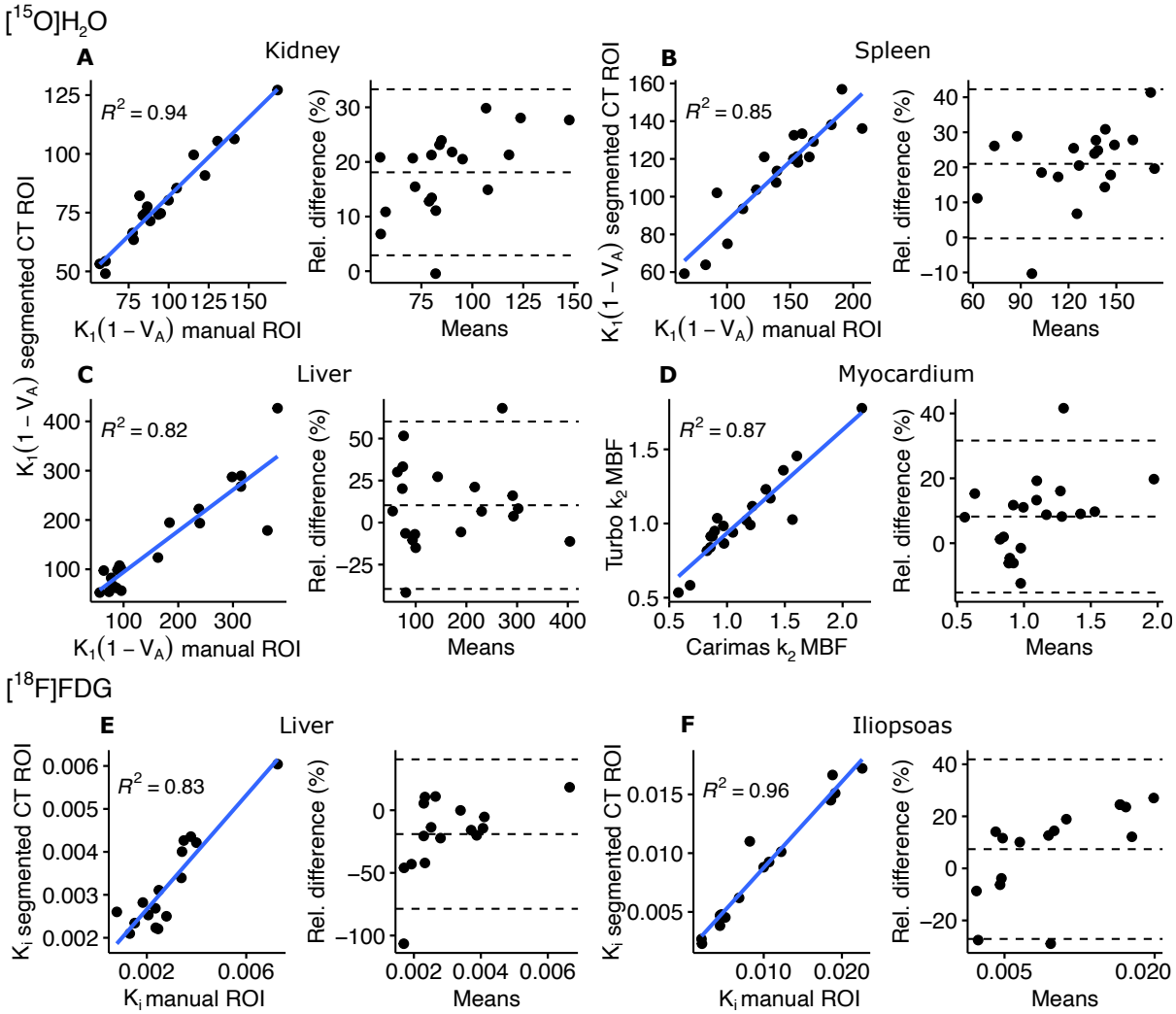

Figure 6. A-C) Scatterplots and Bland-Altman plots illustrating correlation and relative difference between $[^{15}O]H_2O$ parameter estimates of interest in manually drawn ROIs and segmented CT-based ROIs. **D)** Scatterplot and Bland-Altman plot illustrating correlation and relative difference between myocardial blood flow (MBF) measured as k_2 and manually assessed k_2 MBF with left ventricle input and descending aorta IDIF. **E-F)** Scatterplots and Bland-Altman plots illustrating correlation and relative difference between $[^{18}F]$FDG K_i in manually drawn ROIs and segmented CT ROIs.

After reducing the volumes of segmented liver and spleen CT ROIs, the parameter estimates were more closely aligned with the results from manually drawn ROIs (**Figure 7).** Similarly, PET-based clustering gave corresponding estimates in brain as compared to the results of PET-template based processing, but in kidney, the clustered ROI produced higher estimates compared to the manually drawn ROI (**Figure 7).**

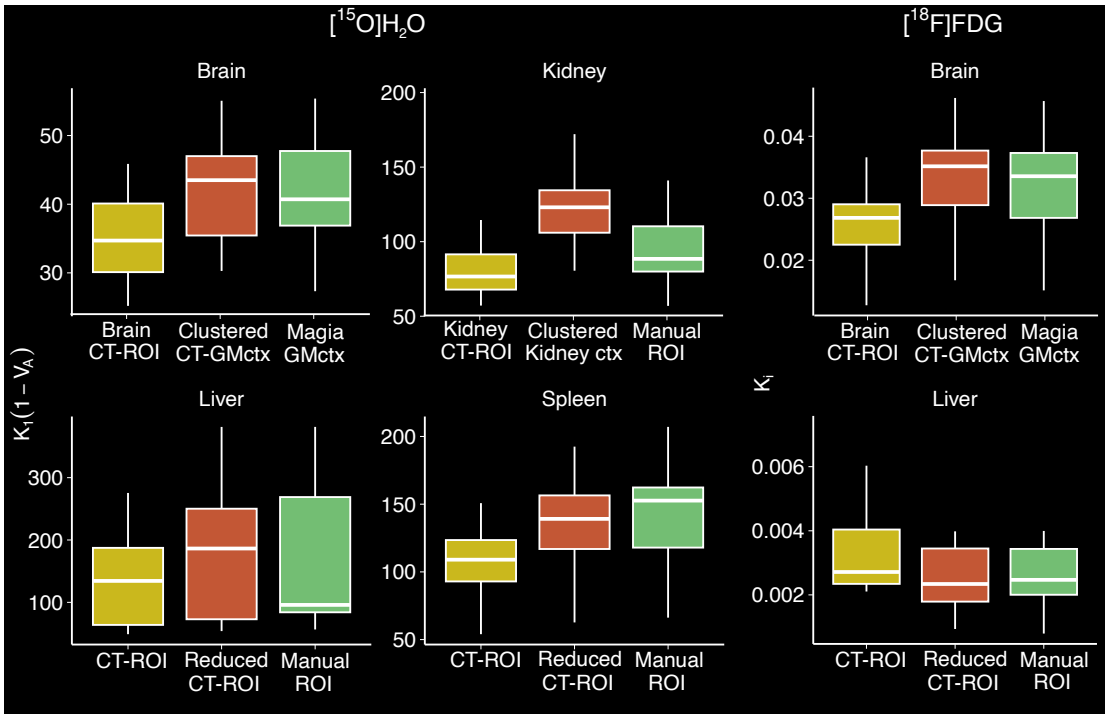

Figure 7. Boxplots illustrating voxel-level [^{15}O]H_2O (n=21) and [^{18}F]FDG (n=16) results using manually drawn ROIs, CT-based ROIs, CT-based ROIs where the volume was reduced (in liver and spleen), and PET-based clustered ROIs (in brain and kidneys).

DISCUSSION

We developed a unified pipeline for total-body PET processing and kinetic modelling and demonstrated that it produces consistent regional estimates of radiotracer uptake for both tested radioligands ([^{15}O]H_2O and [^{18}F]FDG) and that the estimates using automatically delineated input and target ROIs yield consistent estimates with those based on manually drawn ROIs. In contrast with existing pipelines that are limited to specific tissues such as the brain or can handle only a single step of the data preprocessing such as kinetic modelling (Besson and Faure, 2024; Tjerkaski et al., 2020), our pipeline automates the full total-body workflow from pre-processing (image registration, segmentation, and motion correction) to kinetic modelling, making it more versatile and comprehensive compared to the other pipelines (Funck et al., 2018; Gunn et al., 2016; Karjalainen et al., 2020). This complete automatization of the total-body PET data preprocessing and voxel- and region-level kinetic modelling provides significant advantages for the data analysis by improving reproducibility of the analysis through automatization and logging of the processing steps and parameters. It also enables efficient whole-body region-wise studies by removing the operator load through automatization and by reducing inter-operator variability in ROI delineation. Overall, this approach allows standardized large-scale analysis of total-body PET data, paving way for harmonized analysis and data integration in multi-center studies.

Robust automated input delineation and modelling in regional and voxel level

PET data kinetic modelling requires the input function typically obtained either from blood samples or from the image. Blood sampling introduces additional labour to the imaging protocol, but with sufficiently long axial FOV and short imaging frames the input can be derived reliably from the aorta if it is visible in the image (Palard-Novello et al., 2024). Our results confirm that the automatic input delineation implemented in the TURBO pipeline is robust and comparable with manual delineation, and thus it can be reliably used instead of time-consuming manual input ROI drawing.

We also established that the regional outcome measures had high correlation between manually and automatically derived ROIs, and between voxel-level and region-level analyses. Voxel-level [^{15}O]H_2O modelling with basis functions improved alignment with the ROI-based results, when compared to full three-parameter voxel-level model. However, this method requires more processing time because the delay parameter must be estimated for each voxel. Nevertheless, all processing and modelling for one subject was carried out in less than three hours for [^{15}O]H_2O and in two hours for [^{18}F]FDG using a single core from our computational server, and with parallel computing, larger batches can be completed within a day. Altogether, these results show, that TURBO provides reproducible, reliable and computationally fast approach for modelling and investigating whole-body PET data and facilitates the investigation of inter-organ interactions in tissue perfusion and metabolism.

Motion correction

Subject motion is significant source of variation in PET studies affecting to the accuracy of modelling results, particularly in total-body PET where multiple anatomical regions are involved and cannot be restrained as effectively as for example, in brain-only scans. Although controlling the subject motion is crucial to obtain high quality data, involuntary motion, such as breathing and heart motion are still present during image acquisition, as observed in our motion correction results. While the motion during PET scanning and misalignment between CT and PET should ideally be corrected already during image reconstruction, our pipeline also includes post-reconstruction correction methods. To account for complex body movements, we included in our pipeline a diffeomorphic correction method (Sundar et al., 2023), that employs both rigid and nonlinear deformations. Our findings showed high correlation between corrected and uncorrected data, but noticeable differences in absolute values, especially in the kidney and pancreas, which highlights the importance of motion correction.

Although previous research suggests that cardiac motion may require nonlinear correction methods (Lamare et al., 2014), the recent findings have showed that rigid correction methods may be sufficient (Christensen et al., 2023). For practical reasons, we used only rigid motion correction for heart and neighbouring aorta, to minimize altering the original data, and to avoid possible image distortions from diffeomorphic correction. In our pipeline, we use the descending aorta for calculating the IDIF, which can benefit from cardiac motion correction. Based on our results the automated IDIF produced comparable results with the manually derived input without motion correction. The remaining small bias between the results of automated and manual method is likely caused by differences in the input ROI volumes, and because the subject motion is corrected in the automated IDIF. Apart from the input, the other manually drawn ROIs were substantially smaller than the automatically segmented CT-based ROIs, because the manual ROIs were drawn only to a limited number of slices. This likely explains the relative differences between the regional results from automatically derived and

manual ROIs. Because the CT-based segmented ROIs are large entities, the pipeline includes also additional reduced ROIs, which mitigate the effects of subject motion and spill in from other nearby regions. Also, hierarchical clustering of voxel-based parametric maps within a selected region into separate subregions allow to examine the functionally distinct subregions, such as the kidney cortex and medulla.

Limitations

Radiowater model in liver may have issues with parameter identifiability due to dual input model (Becker et al., 2005). Although the validation results were similar between $K_1(1-V_A)$ and distribution volume K_1/k_2, the coefficient of variation was significantly lower for K_1/k_2 and thus it would be preferred measure for quantification. There was also discrepancy between the region-level and voxel-level results in $[^{15}O]H_2O$ data in arteries, lungs and in heart, which likely occurs due to high arterial volume fraction in these regions. Particularly, the K_1 and V_A parameters of 1TCM are highly correlated in regions with to high arterial volume fraction and cannot be reliably estimated (Johnson et al., 2023). In such regions, it is possible to used fixed value (V_A) for arterial volume fraction, which may help to overcome the parameter identifiability issues.

Model fits were generally satisfactory across regions, except in kidneys in $[^{15}O]H_2O$ data, where slight underestimation was observed in the late phase of the scan, likely due to complex tracer kinetics behavior that is not described well by the standard $[^{15}O]H_2O$ model. Since this deviation occurs only in the later part of the scan, perfusion may still be reliably estimated using the earlier data. However, the pipeline is flexible and modular and tailored models with customized inputs can be included, but this warrants further research and careful validation.

Future directions

Future improvements of our pipeline could include the use of pseudo-CT segmentation to reduce possible misalignment between CT and PET images, even though our pipeline already coregisters CT to the PET mean image. This might be useful in e.g. long or multi-scan studies where acquiring additional whole-body reference CT images would increase the radiation load significantly. Another potential development is the spatial normalization of total-body data to a standard template, which is a common approach in brain imaging. Creating such total-body templates for specific tracers would enable voxel-level statistical analysis, which would expand the restricted local regional analysis further to cover the full total-body image volume. Finally, due to the modular structure, the TURBO pipeline can be extended with additional kinetic models.

CONCLUSION

Our results demonstrate that TURBO pipeline offers a fast, accurate, and reproducible solution for analyzing total-body PET perfusion and metabolism at both regional and voxel levels. TURBO provides reproducible, reliable and computationally fast approach for modelling and investigating whole-body PET data and enables interorgan interaction studies in tissue perfusion and metabolism.

DISCLOSURES

This work was supported by European Research Council (Advanced Grant #101141656 to LN), Jane and Aatos Erkko Foundation, the Finnish Foundation for Cardiovascular Research, Finnish State Research Funding (VRT), Finnish Cultural Foundation, InFLAMES research flagship and Gyllenberg's Stiftelse. Dr. Knuuti received consultancy fees from GE Healthcare and Synektik and speaker fees from Siemens Healthineers, outside of the submitted work.

ACKNOWLEDGEMENTS

REFERENCES

Becker, G.A., Müller-Schauenburg, W., Spilker, M.E., Machulla, H.J., Piert, M., 2005. A priori identifiability of a one-compartment model with two input functions for liver blood flow measurements. Phys. Med. Biol. 50, 1393. https://doi.org/10.1088/0031-9155/50/7/004

Besson, F.L., Faure, S., 2024. PET KinetiX-A Software Solution for PET Parametric Imaging at the Whole Field of View Level. J. imaging informatics Med. 37, 842–850. https://doi.org/10.1007/S10278-023-00965-Z

Christensen, N.L., Nordström, J., Madsen, S., Madsen, M.A., Gormsen, L.C., Kero, T., Lubberink, M., Tolbod, L.P., 2023. Detection and correction of patient motion in dynamic 15O-water PET MPI. J. Nucl. Cardiol. 30, 2736–2749. https://doi.org/10.1007/S12350-023-03358-5

DeFronzo, R.A., Tobin, J.D., Andres, R., 1979. Glucose clamp technique: a method for quantifying insulin secretion and resistance. https://doi.org/10.1152/ajpendo.1979.237.3.E214 6. https://doi.org/10.1152/AJPENDO.1979.237.3.E214

Funck, T., Larcher, K., Toussaint, P.J., Evans, A.C., Thiel, A., 2018. APPIAN: Automated Pipeline for PET Image Analysis. Front. Neuroinform. 12, 408902. https://doi.org/10.3389/FNINF.2018.00064/BIBTEX

Greve, D.N., Svarer, C., Fisher, P.M., Feng, L., Hansen, A.E., Baare, W., Rosen, B., Fischl, B., Knudsen, G.M., 2014. Cortical surface-based analysis reduces bias and variance in kinetic modeling of brain PET data. Neuroimage 92, 225–236. https://doi.org/10.1016/J.NEUROIMAGE.2013.12.021

Gunn, R., Coello, C., Medicine, G.S.-J. of N., 2016, U., 2016. Molecular imaging and kinetic analysis toolbox (MIAKAT)-a quantitative software package for the analysis of PET neuroimaging data. J. Nucl. Med. 57, 1928.

Johnson, L.C., Guerraty, M.A., Moore, S.C., Metzler, S.D., 2023. Determining the Effect of Cardiac Blood Volume on Accuracy of Uptake Rate Constants by Simulation. Phys. Med. Biol. 68, 10.1088/1361-6560/ace0f1. https://doi.org/10.1088/1361-6560/ACE0F1

Karjalainen, T., Tuisku, J., Santavirta, S., Kantonen, T., Bucci, M., Tuominen, L., Hirvonen, J., Hietala, J., Rinne, J.O., Nummenmaa, L., 2020. Magia: Robust Automated Image Processing and Kinetic Modeling Toolbox for PET Neuroinformatics. Front. Neuroinform. 14, 3. https://doi.org/10.3389/fninf.2020.00003

Kety, S.S., Schmidt, C.F., 1948. The nitrous oxide method for the quantitative determination of cerebral blood flow in man: theory, procedure and normal values. J. Clin. Invest. 27, 476. https://doi.org/10.1172/JCI101994

Knuuti, J., Tuisku, J., Kärpijoki, H., Iida, H., Maaniitty, T., Latva-Rasku, A., Oikonen, V., Nesterov, S. V., Teuho, J., Jaakkola, M.K., Klén, R., Louhi, H., Saunavaara, V., Nuutila, P., Saraste, A., Rinne, J., Nummenmaa, L., 2023. Quantitative Perfusion Imaging with Total-Body PET. J. Nucl. Med. 64, 11S-19S. https://doi.org/10.2967/JNUMED.122.264870

Kudomi, N., Koivuviita, N., Liukko, K.E., Oikonen, V.J., Tolvanen, T., Iida, H., Tertti, R., Metsärinne, K., Iozzo, P., Nuutila, P., 2009. Parametric renal blood flow imaging using [15O]H2O and PET. Eur. J. Nucl. Med. Mol. Imaging 36, 683–691. https://doi.org/10.1007/S00259-008-0994-8

Kudomi, N., Slimani, L., Järvisalo, M.J., Kiss, J., Lautamäki, R., Naum, G.A., Savunen, T., Knuuti, J., Iida, H., Nuutila, P., Iozzo, P., 2008. Non-invasive estimation of hepatic blood perfusion from H2 15O PET images using tissue-derived arterial and portal input functions. Eur. J. Nucl. Med. Mol. Imaging 35, 1899–1911. https://doi.org/10.1007/S00259-008-0796-Z

Lamare, F., Le Maitre, A., Dawood, M., Schäfers, K.P., Fernandez, P., Rimoldi, O.E., Visvikis, D., 2014. Evaluation of respiratory and cardiac motion correction schemes in dual gated PET/CT cardiac imaging. Med. Phys. 41. https://doi.org/10.1118/1.4881099

Lawson, C.L., Hanson, R.J., 1995. Solving Least Squares Problems, Solving Least Squares Problems. Society for Industrial and Applied Mathematics. https://doi.org/10.1137/1.9781611971217

Li, X., Morgan, P.S., Ashburner, J., Smith, J., Rorden, C., 2016. The first step for neuroimaging data analysis: DICOM to NIfTI conversion. J. Neurosci. Methods 264, 47–56. https://doi.org/10.1016/J.JNEUMETH.2016.03.001

Nesterov, S. V., Han, C., Mäki, M., Kajander, S., Naum, A.G., Helenius, H., Lisinen, I., Ukkonen, H., Pietilä, M., Joutsiniemi, E., Knuuti, J., 2009. Myocardial perfusion quantitation with 15O-labelled water PET: High reproducibility of the new cardiac analysis software (Carimas^{TM}). Eur. J. Nucl. Med. Mol. Imaging 36, 1594–1602. https://doi.org/10.1007/S00259-009-1143-8/METRICS

Nordstrom, J., Kero, T., Lindstrom, E., Sigfridsson, J., Sorensen, J., Lubberink, M., 2024. Cardiac 15O-water PET motion correction using patient specific synthetic dynamic images. Eur. Hear. J. - Cardiovasc. Imaging 25. https://doi.org/10.1093/EHJCI/JEAE142.096

Palard-Novello, X., Visser, D., Tolboom, N., Smith, C.L.C., Zwezerijnen, G., van de Giessen, E., den Hollander, M.E., Barkhof, F., Windhorst, A.D., van Berckel, B.N.M., Boellaard, R., Yaqub, M., 2024. Validation of image-derived input function using a long axial field of view PET/CT scanner for two different tracers. EJNMMI Phys. 11, 1–13. https://doi.org/10.1186/S40658-024-00628-0/FIGURES/5

Patlak, C.S., Blasberg, R.G., Fenstermacher, J.D., 1983. Graphical evaluation of blood-to-brain transfer constants from multiple-time uptake data. J. Cereb. Blood Flow Metab. 3, 1–7. https://doi.org/10.1038/JCBFM.1983.1

Phelps, M.E., Huang, S.C., Hoffman, E.J., Selin, C., Sokoloff, L., Kuhl, D.E., 1979. Tomographic measurement of local cerebral glucose metabolic rate in humans with (F-18)2-fluoro-2-deoxy-D-glucose: Validation of method. Ann. Neurol. 6, 371–388. https://doi.org/10.1002/ana.410060502

Prenosil, G.A., Sari, H., Fürstner, M., Afshar-Oromieh, A., Shi, K., Rominger, A., Hentschel, M., 2022. Performance Characteristics of the Biograph Vision Quadra PET/CT System with a Long Axial Field of View Using the NEMA NU 2-2018 Standard. J. Nucl. Med. 63, 476–484. https://doi.org/10.2967/JNUMED.121.261972

Rainio, O., Han, C., Teuho, J., Nesterov, S. V., Oikonen, V., Piirola, S., Laitinen, T., Tättäläinen, M., Knuuti, J., Klén, R., 2023. Carimas: An Extensive Medical Imaging

Data Processing Tool for Research. J. Digit. Imaging 1–9. https://doi.org/10.1007/S10278-023-00812-1/FIGURES/5

Sundar, L.K.S., Lassen, M.L., Gutschmayer, S., Ferrara, D., Calabrò, A., Yu, J., Kluge, K., Wang, Y., Nardo, L., Hasbak, P., Kjaer, A., Abdelhafez, Y.G., Wang, G., Cherry, S.R., Spencer, B.A., Badawi, R.D., Beyer, T., Muzik, O., 2023. Fully Automated, Fast Motion Correction of Dynamic Whole-Body and Total-Body PET/CT Imaging Studies. J. Nucl. Med. jnumed.122.265362. https://doi.org/10.2967/JNUMED.122.265362

Tjerkaski, J., Cervenka, S., Farde, L., Matheson, G.J., 2020. Kinfitr — an open-source tool for reproducible PET modelling: validation and evaluation of test-retest reliability. EJNMMI Res. 10. https://doi.org/10.1186/s13550-020-00664-8

Tzourio-Mazoyer, N., Landeau, B., Papathanassiou, D., Crivello, F., Etard, O., Delcroix, N., Mazoyer, B., Joliot, M., 2002. Automated Anatomical Labeling of Activations in SPM Using a Macroscopic Anatomical Parcellation of the MNI MRI Single-Subject Brain. Neuroimage 15, 273–289. https://doi.org/10.1006/NIMG.2001.0978

Wasserthal, J., Breit, H.C., Meyer, M.T., Pradella, M., Hinck, D., Sauter, A.W., Heye, T., Boll, D.T., Cyriac, J., Yang, S., Bach, M., Segeroth, M., 2023. TotalSegmentator: Robust Segmentation of 104 Anatomic Structures in CT Images. Radiol. Artif. Intell. 5. https://doi.org/10.1148/RYAI.230024/ASSET/IMAGES/LARGE/RYAI.230024.FIG6.JPEG

Ziegler, S.I., Haberkorn, U., Byrne, H., Tong, C., Schosser, R., Krieter, H., Kaja, S., Richolt, J.A., Lammertsma, A.A., Price, P., 1996. Measurement of liver blood flow using oxygen-15 labelled water and dynamic positron emission tomography: Limitations of model description. Eur. J. Nucl. Med. 23, 169–177. https://doi.org/10.1007/BF01731841/METRICS

Supplementary information

TURBO: Automated Total-body PET Image Processing and Kinetic Modeling Toolbox

Jouni Tuisku*[1,2], Santeri Palonen*[1,2], Henri Kärpijoki[1,2], Aino Latva-Rasku[1,2], Nelli Tuomola[1,2], Harri Harju[1,2], Sergey Nesterov[1,2], Vesa Oikonen[1,2], Hidehiro Iida[1,2], Jarmo Teuho[1,2], Chunlei Han[1,2], Tomi Karjalainen[1,2], Anna K. Kirjavainen[1,4], Johan Rajader[1,3], Riku Klen[1,2], Pirjo Nuutila[1,2], Juhani Knuuti[1,2], Lauri Nummenmaa[1,2,5]

[1]Turku PET Centre, University of Turku, Turku, Finland
[2]Turku PET Centre, Turku university hospital, Turku, Finland
[3]Turku PET Centre, Accelerator Laboratory, Åbo Akademi University, Turku, Finland
[4]Turku PET Centre, Radiopharmaceutical Chemistry Laboratory, University of Turku, Turku, Finland.
[5]Department of Psychology, University of Turku, Turku, Finland

*contributed equally to this study

Methods

One-tissue compartmental model (1TCM) (Kety and Schmidt, 1948) is defined using the following differential equation:

$$\frac{dC_T(t)}{dt} = K_1 C_A(t) - k_2 C_T(t) \quad (1).$$

Assuming that initial concentration in tissue compartment is zero ($C_T(0) = 0$), eq (1) can be integrated to provide the tissue concentration at time T:

$$C_T(T) = K_1 \int_0^T C_A(t)dt - k_2 \int_0^T C_T(t)dt \quad (2).$$

The measured PET radioactivity concentration in tissue is contaminated by spillover from adjacent blood vessels C_B and vascular volume V_B inside the measured region $C_{PET}(t)$, which can be formulated as follows:

$$C_{PET}(t) = V_B C_B(t) + C_T(t) \quad (3).$$

Substituting $C_T(t)$ in eq (3) with eq (2) gives the following equation:

$$C_{PET}(t) = V_B C_B(t) + K_1 \int_0^T C_A(t)dt - k_2 \int_0^T C_T(t)dt \quad (4).$$

Integration and rearrangement of eq (3) gives

$$\int_0^T C_T(t)dt = \int_0^T C_{PET}(t)dt - V_B \int_0^T C_B(t)dt \quad (5),$$

which is then substituted in eq (4), providing the following equation:

$$C_{PET}(t) = V_B C_B(t) + K_1 \int_0^T C_A(t)dt - k_2 \int_0^T C_{PET}(t)dt + k_2 V_B \int_0^T C_B(t)dt \quad (6).$$

If the radioactivity concentration in blood can be represented by the model input function, as is the case with [^{15}O]H_2O, then $C_B(t) = C_A(t)$ and $V_B = V_A$, and then eq (6) simplifies to eq (7):

$$C_{PET}(t) = V_A C_A(t) + (K_1 + V_A k_2) \int_0^T C_A(t)dt - k_2 \int_0^T C_{PET}(t)dt \quad (7).$$

Equation (7) is a multilinear equation $y = p_1\, x_1 + \ p_2 x_2 + \ p_3 x_3$, where the coefficients

$$V_A = p_1$$
$$k_2 = p_3$$
$$K_1 = p_2 - V_A k_2$$

can be estimated with least squares method (Oikonen, 2003). Particularly, non-negative least squares (NNLS, Lawson and Hanson, 1995) is well-suited method for estimating the coefficients.

The differential equation (1) can also be directly solved using convolution:

$$C_T(t) = (1 - V_A)K_1 C_A * e^{-k_2 t} \ (8),$$

where $C_T(t)$ is the radioactivity concentration in tissue, $C_A(t)$ is the arterial input function and * is the convolution operator. By denoting $C_B(t) = C_A(t)$ and $V_B = V_A$, and substituting eq (8) to eq (3), we get

$$C_{PET}(t) = (1 - V_A)K_1 C_A * e^{-k_2 t} + V_A C_A(t) \ (9).$$

The equation (9) can be rewritten as a multilinear equation:

$$C_T(t) = \ \theta_1 B(k_2, t) + \theta_2 C_A(t),$$

using basis functions

$$B(k_2, t) = C_A(t) * e^{-k_2 t},$$

and where the coefficients

$$\theta_1 = (1 - V_A)K_1$$
$$\theta_2 = V_A$$

can be estimated with least squares method (Kudomi et al., 2008).

Data acquisition

[^{15}O]H_2O PET data were acquired for 280 s following 359.6 ± 23.8 MBq bolus injection over 10–15 seconds (Radiowater Generator, Hidex Oy, Finland). Imaging started 30 seconds after the start of the bolus injection. The data were reconstructed into 24 frames (14 × 5 s, 3 × 10 s, 3 × 20 s, 4 × 30 s) using an image matrix of 220 × 220 × 380 and a voxel size of 1.65 × 1.65 × 2.80 mm³. Reconstruction was performed with an ordered-subsets expectation maximization (OSEM) algorithm (3 iterations, 5 subsets) using point-spread function and time-of-flight modelling, and included corrections for decay, randoms, attenuation, and scatter.

[^{18}F]FDG PET were acquired 55 minutes during euglycemic hyperinsulinemic clamp after 171.8 ± 8.8 MBq bolus injection. Before the scan, two venous catheters were inserted in the opposite forearms, one for the insulin and glucose infusions and for injecting [^{18}F]FDG, and the other for collecting venous blood samples, arterialised by placing a hot water bottle distally on the arm. After the collection of fasting plasma blood samples, hyperinsulinemic, euglycemic clamp was started (DeFronzo et al., 1979). Insulin (Actrapid, Novo Nordisk A/S, Bagsvaerd, Denmark) was administered with a reduced dose of 37 mU/min/m^2 of body surface area, and a variable rate of 20% glucose was infused based on plasma glucose measurements performed every 5–10 min to maintain euglycemia (plasma glucose 5.0 mmol/L). Data were reconstructed using OSEM algorithm (4 iterations, 5 subsets) using point-spread function and time-of-flight modelling, and included corrections for decay, randoms, attenuation, and scatter. The data were reconstructed into 34 frames (l2 x 5s, 6 x10s, 6 x 20s, 2 x 60s, 2 x 120s, 4 x 300s, 2x 600s) with 440 x 440 x 354 matrix size and 1.65 x 1.65 x 3.0 mm^3 voxel-size.

Prior to the PET image acquisition, the total-body CT images were acquired and reconstructed to 512 × 512 × 380 image matrix with a voxel size of 0.977 × 0.977 × 2.80 mm^3.

Quality control plots for representative [^{15}O]H_2O subject:

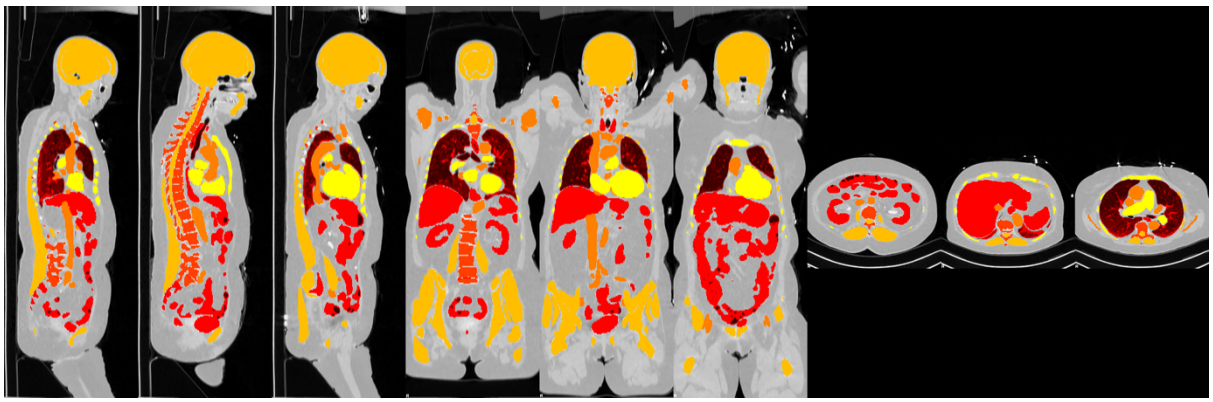

QC figure 1. CT segments overlaid on CT image.

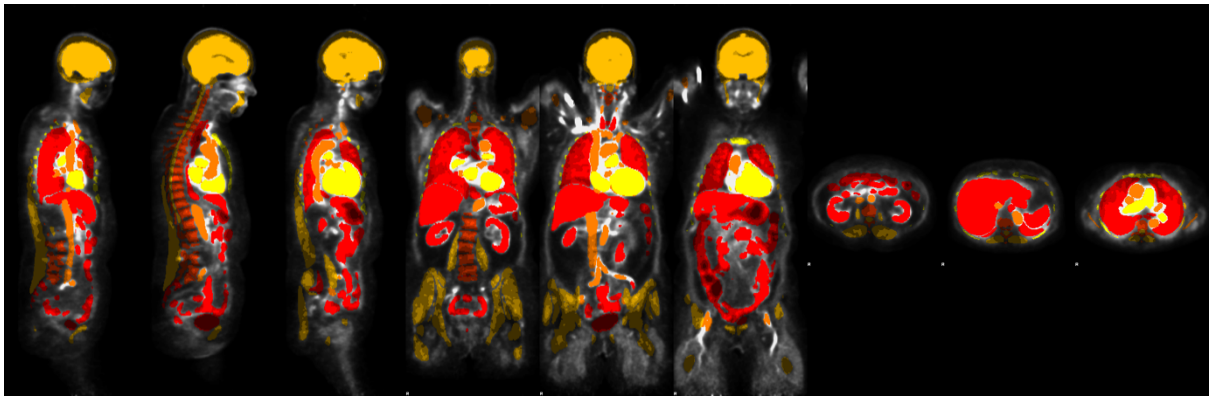

QC figure 2. CT segments overlaid on mean PET image.

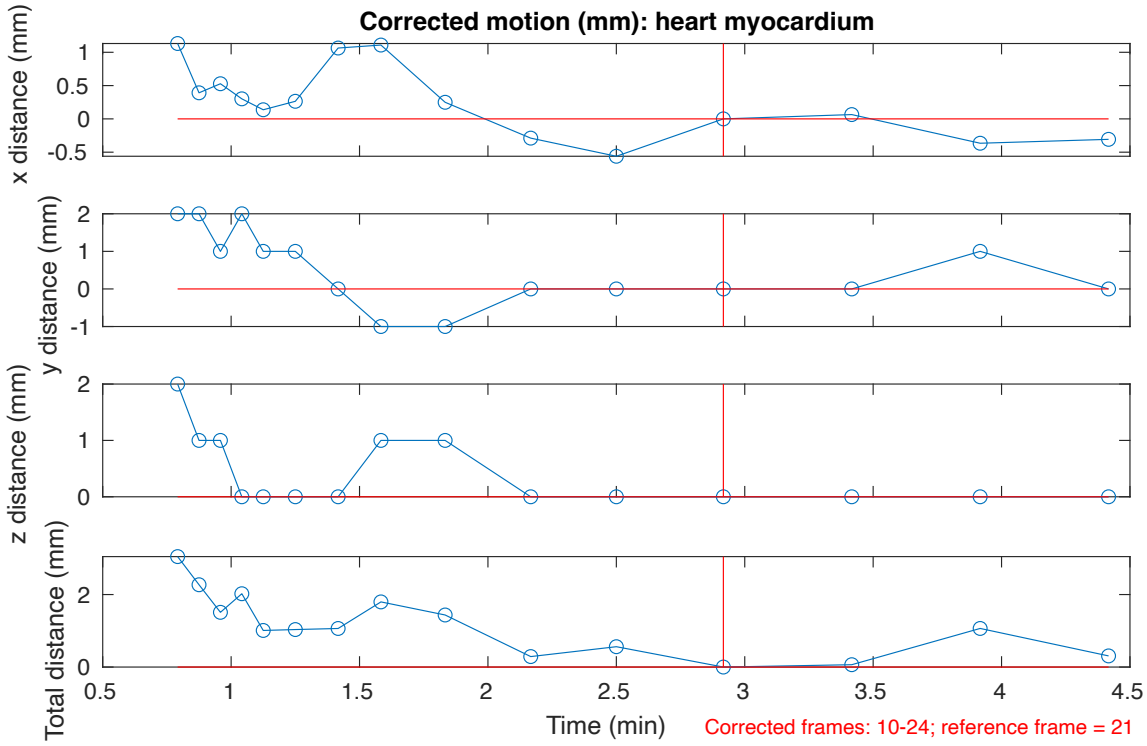

QC figure 3. Corrected motion for heart myocardium.

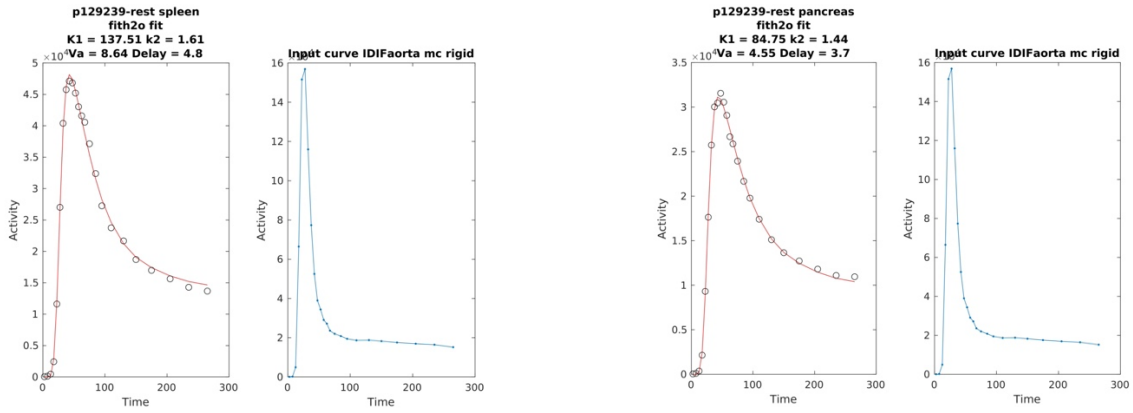

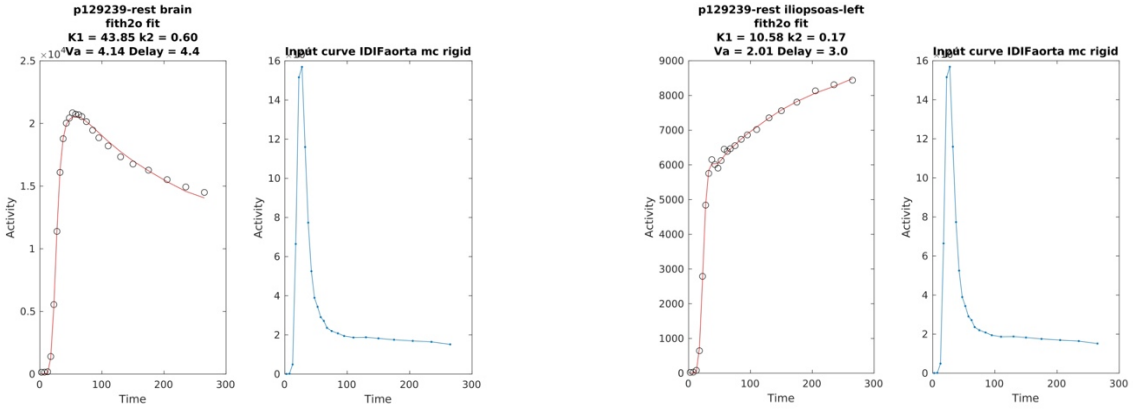

QC figure 4. Example model fits

Results

Supplementary tables 1-4 and figures S1-S6.

Supplementary Table 1. Typical TURBO-pipeline processing times for representative cases of [^{15}O]H_2O and [^{18}F]FDG data.

Process	[^{15}O]H_2O processing time (min)	[^{18}F]FDG processing time (min)
CT segmentation	5	7
CT coregistration	7	12
PET motion correction	45	73
TAC extraction	1	6
Input data processing	2	3
Quality control	2	3
ROI-level modelling	6	4
Voxel-level modelling	85	2
Magia brain processsing	4	6
Magia brain modelling	3	1
Turbo processing total time	66	108
Turbo modelling total time	94	6
Total running time	160	115

Supplementary Table 2. Input ROI volumes.

	$[^{15}O]H_2O$			$[^{18}F]FDG$		
Measure	**Manual input**	**IDIF**	**p-value***	**Manual input**	**IDIF**	**p-value***
Volume (ml)	4.0 (2.2)	4.0 (0.7)	0.99	8.2 (2.0)	4.5 (0.9)	p < 0.01
AUC/1000	120.7 (28.2)	120.4 (28.8)	0.53	167.5 (29.2)	167.3 (30.1)	0.84
Dice coefficient	0.5 (0.1)			0.5 (0.1)		

*paired t-test

Supplementary Table 3. Corrected frame-wise motion (mm) for selected six regions in $[^{15}O]H_2O$ and $[^{18}F]FDG$ test data.

	$[^{15}O]H_2O$		$[^{18}F]FDG$	
Region	Mean motion (mm) mean (sd)	Max motion (mm) mean (sd)	Mean motion (mm) mean (sd)	Max motion (mm) mean (sd)
Brain GMctx	0.6 (0.6)	2.1 (1.0)	2.3 (0.9)	6.1 (2.0)
Left iliopsoas	2.4 (0.7)	4.7 (1.2)	3.8 (1.9)	6.9 (3.3)
Liver	5.0 (1.9)	18.7 (7.8)	4.3 (1.9)	18.5 (17.6)
Right kidney	5.1 (1.5)	16.4 (7.5)	4.1 (1.5)	9.9 (3.1)
Spleen	3.1 (0.8)	6.5 (3.3)	3.9 (1.2)	8.0 (2.6
Pancreas	4.4 (1.4)	11.1 (6.1)	4.6 (1.4)	13.5 (6.1)

Supplementary Table 4. Volumes of manually drawn ROIs and segmented CT ROIs.

Radioligand	**Region**	**Segmented CT volume (ml) mean (sd)**	**Manual ROI volume (ml) mean (sd)**
$[^{15}O]H_2O$	Liver	1510.7 (464.6)	42.4 (20.6)
	Spleen	181.2 (63.7)	13.9 (5.3)
	Kidney	382.6 (137.0)	47.4 (16.9)
$[^{18}F]FDG$	Liver	1639.8 (330.5)	29.6 (12.9)
	Iliopsoas	578.9 (92.3)	11.6 (4.5)

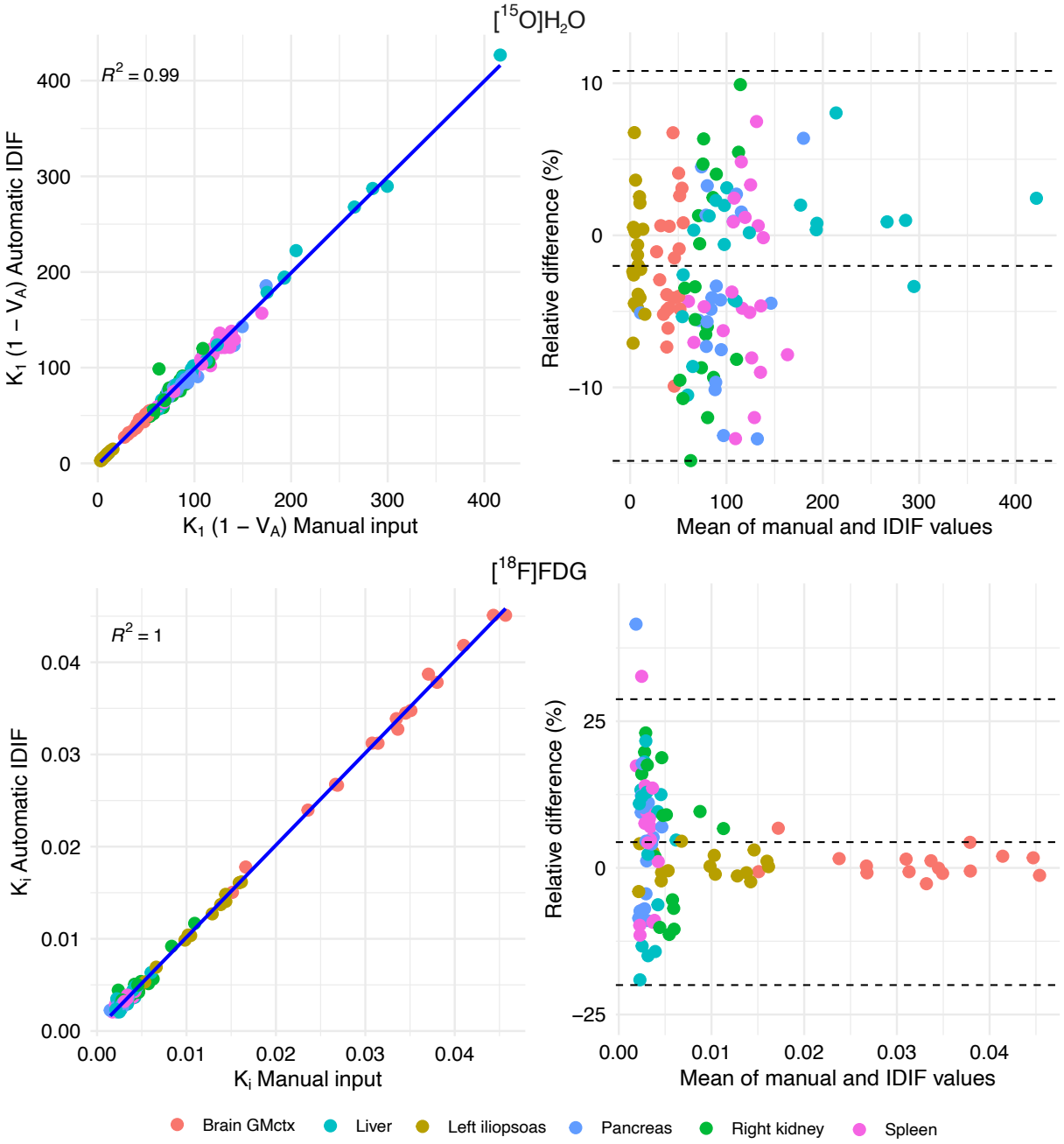

Figure S1. Pearson's correlation and Bland-Altman plots of parameter estimates ($K_1(1-V_A)$ for $[^{15}O]H_2O$ and patlak K_i for $[^{18}F]FDG$) in six example regions, calculated using manually derived, and image derived input (IDIF) from descending aorta.

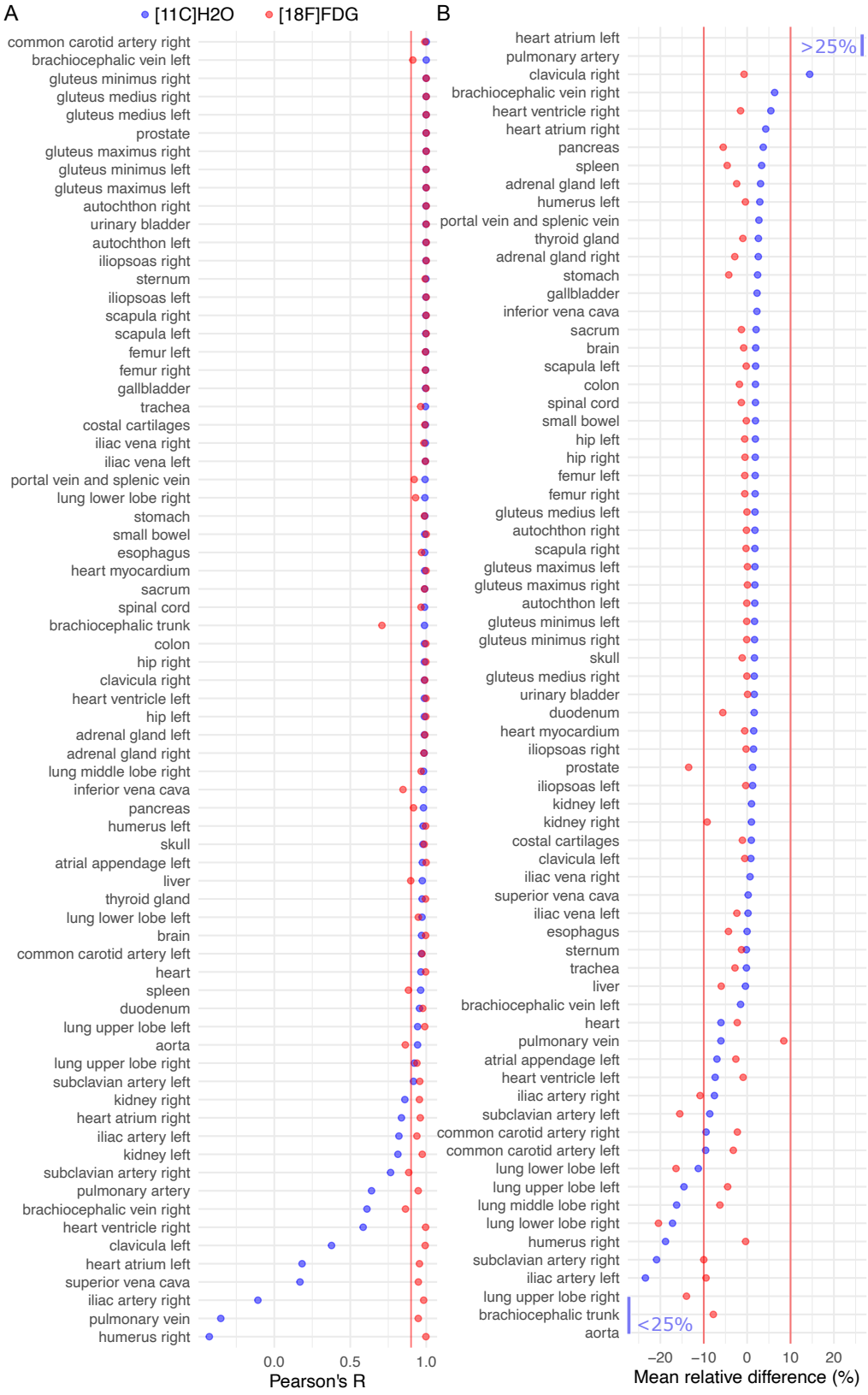

Figure S2. A) Pearson's correlation of model parameter estimates calculated using manually derived, and image derived input (IDIF) from descending aorta. **B)** Mean relative differences between model parameter estimates calculated using manually derived, and image derived input (IDIF) from descending aorta. Regional $[^{15}O]H_2O$ $K_1(1\text{-}V_A)$ estimates are coloured in blue and $[^{18}F]$FDG K_i estimates in red.

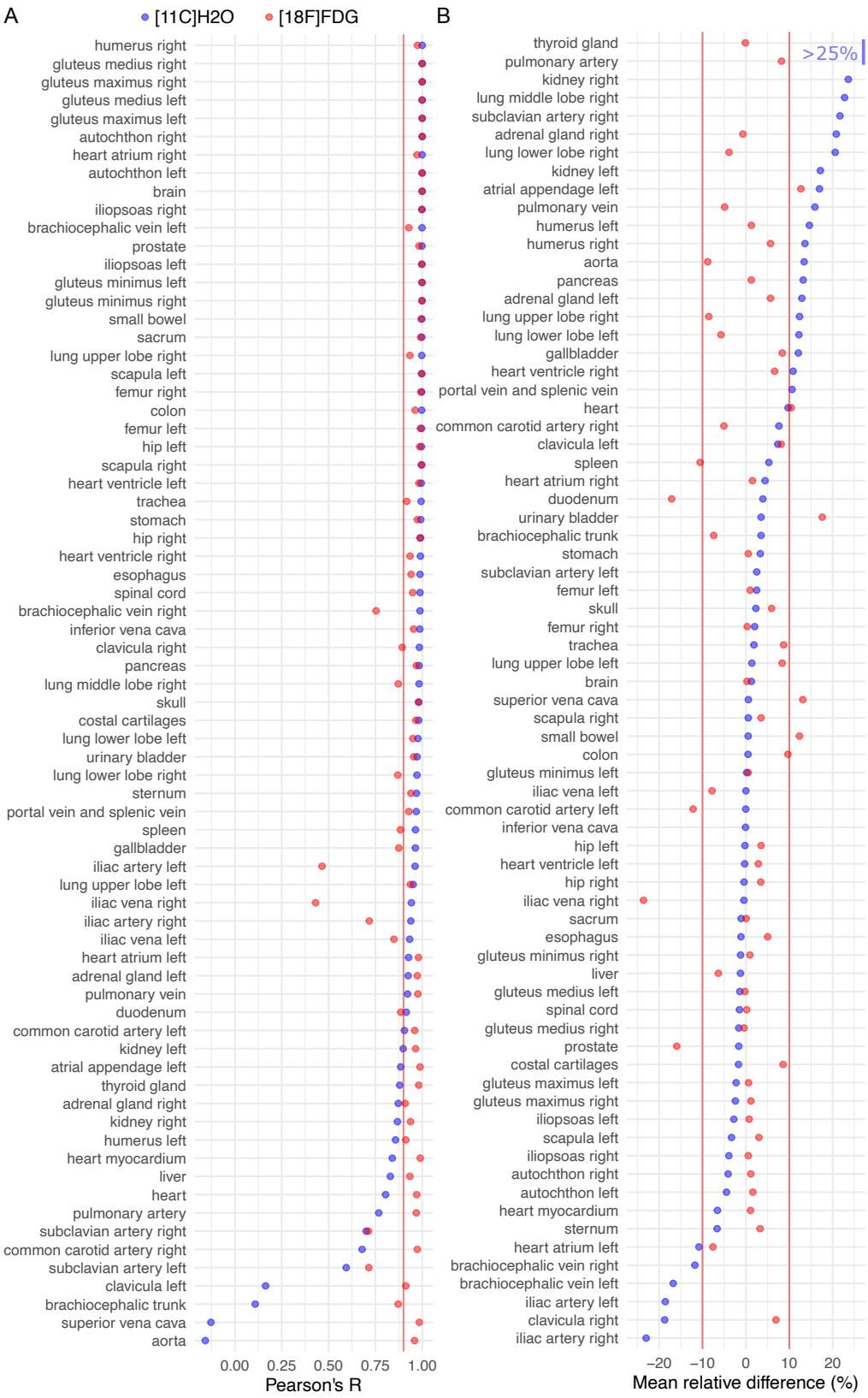

Figure S3. A) Pearson's correlation of model parameter estimates calculated using data with and without motion correction. **B)** Mean relative differences between model parameter estimates calculated using data with and without motion correction. Regional [^{15}O]H_2O $K_1(1-V_A)$ estimates are coloured in blue and [^{18}F]FDG K_i estimates in red.

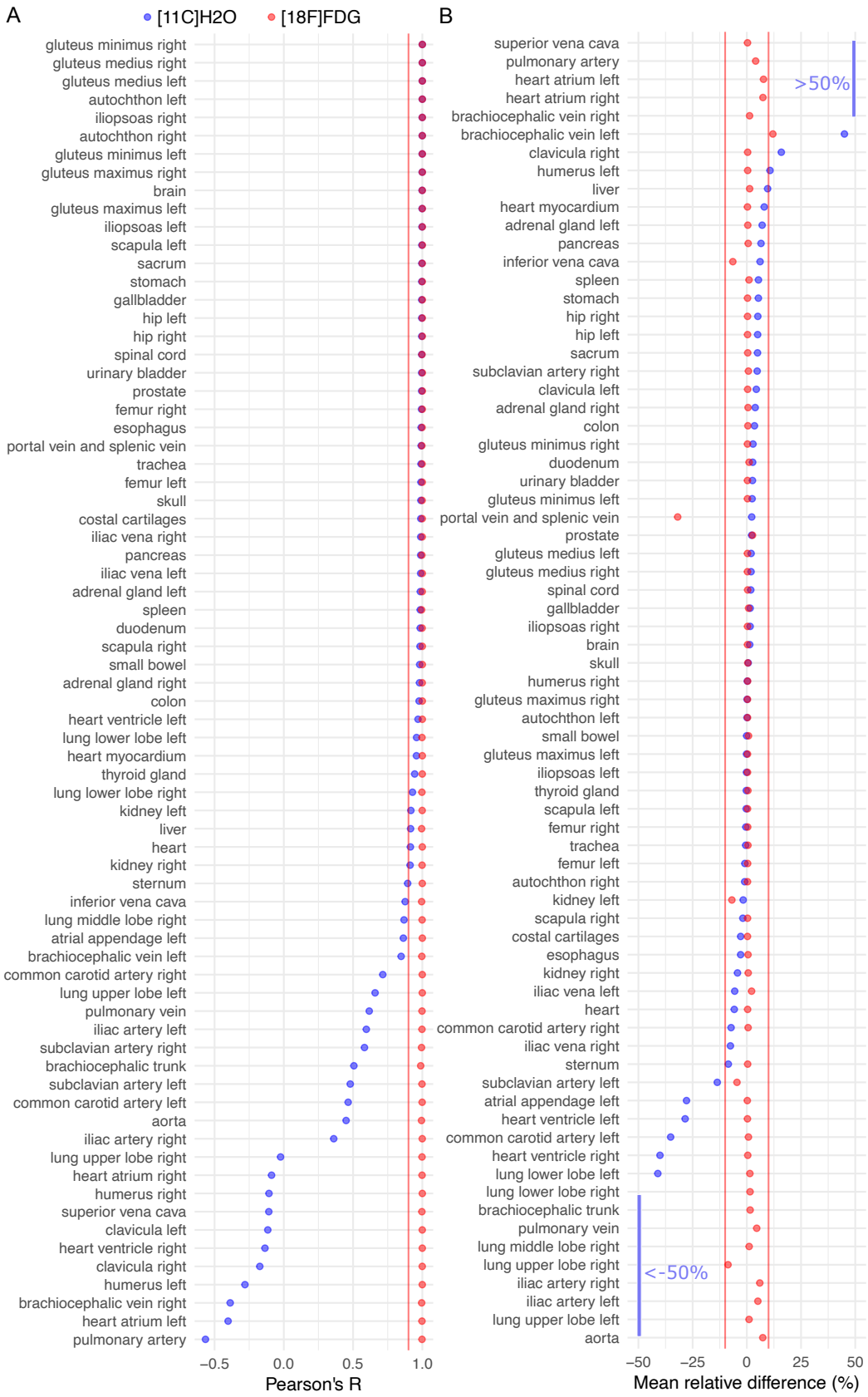

Figure S4. A) Pearson's correlation of model parameter estimates calculated using ROI- and voxel level modelling. Basis function method was used at voxel-level. **B)** Mean relative differences between model parameter estimates calculated using ROI- and voxel level modelling**.** Regional [^{15}O]H_2O $K_1(1\text{-}V_A)$ estimates are coloured in blue and [^{18}F]FDG K_i estimates in red.

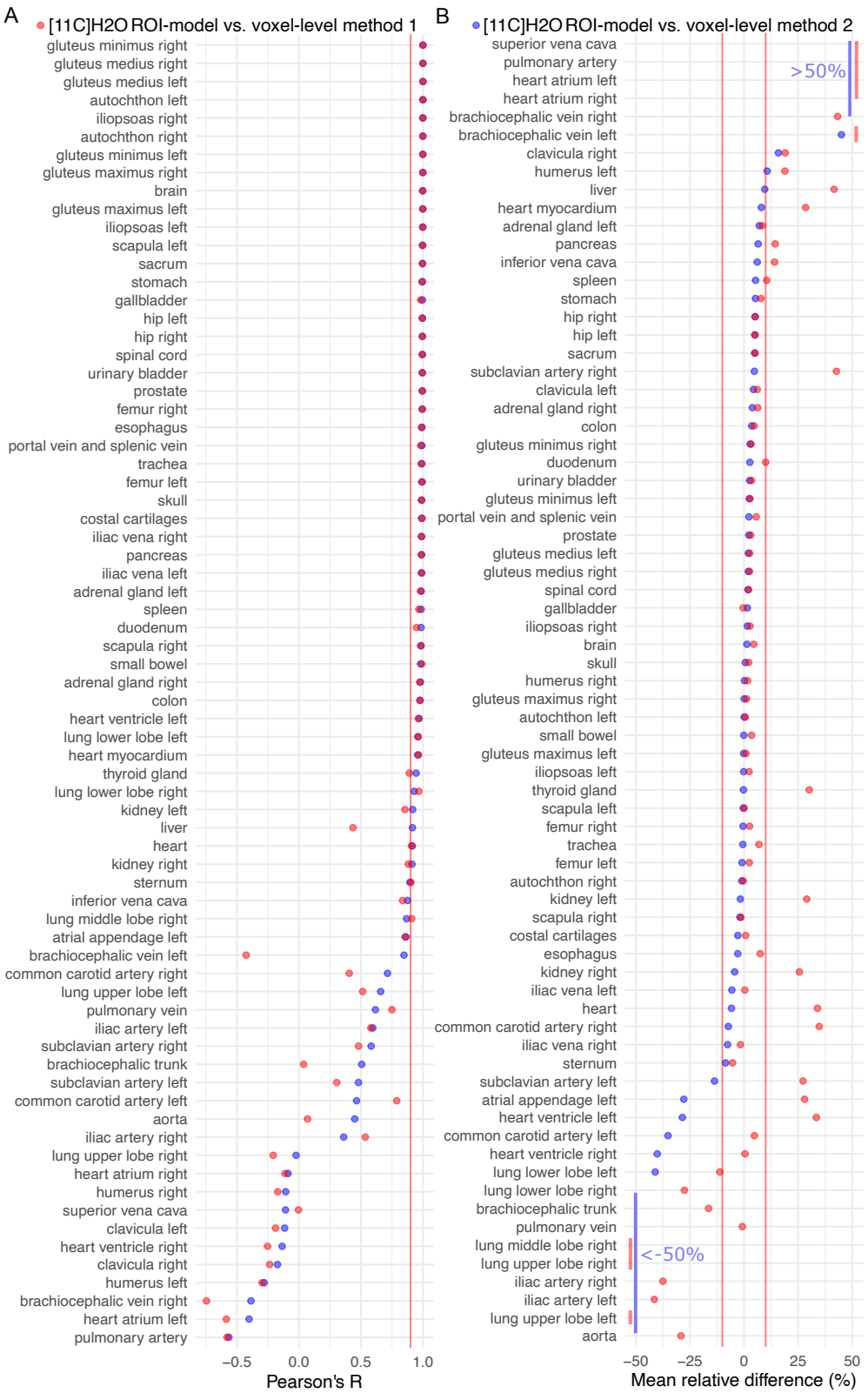

Figure S5. A) Pearson's correlation of [^{15}O]H_2O 1-tissue compartment model $K_1(1\text{-}V_A)$ estimates calculated using ROI- and voxel level modelling. **B)** Mean relative differences between [^{15}O]H_2O 1-tissue compartment model $K_1(1\text{-}V_A)$ parameter estimates calculated using ROI- and voxel level modelling. Red markers show the comparison between a three-parameter (K_1, k_2, V_A) ROI-level model and three-parameter voxel-level model (method 1), and blue markers show the comparison between three-parameter ROI level-model and basis function voxel-level model (method 2) with two estimated model parameters (K_1, V_A).

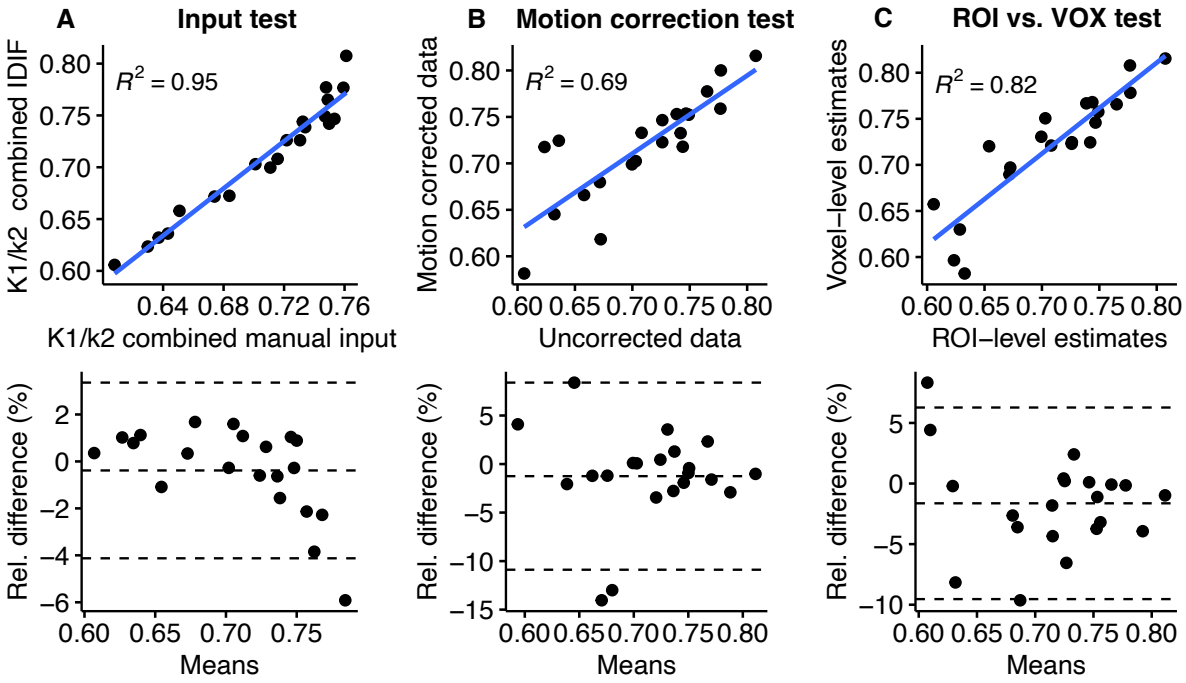

Figure S6. Scatterplots and Bland-Altman plots illustrating correlation and relative difference between [^{15}O]H_2O liver partition coefficient of water ($p=K_1/k_2$) estimates, where **A**) parameter estimates obtained with manual input are compared with parameter estimates calculated using IDIF, **B**) parameter estimates calculated using uncorrected data are compared with parameter estimates calculated using motion corrected data, and **C**) ROI-level parameter estimates are compared with voxel-level parameter estimates.

References:

Kety, S.S., Schmidt, C.F., 1948. The nitrous oxide method for the quantitative determination of cerebral blood flow in man: theory, procedure and normal values. J. Clin. Invest. 27, 476. https://doi.org/10.1172/JCI101994

Kudomi, N., Slimani, L., Järvisalo, M.J., Kiss, J., Lautamäki, R., Naum, G.A., Savunen, T., Knuuti, J., Iida, H., Nuutila, P., Iozzo, P., 2008. Non-invasive estimation of hepatic blood perfusion from H215O-PET images using tissue-derived arterial and portal input functions. Eur. J. Nucl. Med. Mol. Imaging 35, 1899. https://doi.org/10.1007/S00259-008-0796-Z

Lawson, C.L., Hanson, R.J., 1995. Solving Least Squares Problems, Solving Least Squares Problems. Society for Industrial and Applied Mathematics. https://doi.org/10.1137/1.9781611971217

Oikonen, V., 2003. Multilinear solution for 4-compartment model: I. Tissue compartments in series. https://doi.org/10.13140/2.1.1598.9762